HEAVY ION ORBITING AND REGGE POLES (II)

F. CARSTOIU[1], M. LASSAUT[2], L. TRACHE[1], V. BALANICA[1]

[1]National Institute for Nuclear Physics and Engineering,
P.O.Box MG-6, RO-077125 Bucharest-Magurele, Romania
[2]Institut de Physique Nucléaire, CNRS-IN2P3, Univ. Paris-Sud,
Université Paris-Saclay, 91406 Orsay Cedex, France

Received September 8, 2015

We discuss two specific examples of heavy ion orbiting. A first example, α+^{16}O at 54.1 MeV reaction dominated by strong optical potentials shows all characteristics of a strongly refractive scattering: Fraunhofer cross over at very forward angles, deep Airy oscillation, rainbow bump, significant increase of the cross section at large angles. We demonstrate semiclassically that this in fact is a typical orbiting reaction. In a second example, α+^{28}Si at 18.0 MeV, we describe a special kind of heavy ion orbiting-butterfly scattering, with diffractive oscillations in the entire physical angular range, determined by Regge pole dominance.

Key words: G-matrix effective interactions, folding potentials, WKB, Regge poles.

PACS: 24.10.Ht, 25.55.Ci, 25.70.Ef.

1. INTRODUCTION

Significant progress has been achieved during the last decades in our understanding of the optical potential between light heavy-ions as a consequence of the measurement of accurate and extensive elastic differential cross sections. In many cases angular distributions have been measured to sufficiently large angles and thus the reaction mechanism gouverning the interaction could be identified with precision, ranging from diffraction due to strong absorption to refractive effects (rainbows). A good understanding of all phenomena occurring in the elastic nucleus-nucleus scattering, which are used typically to extract OMP, and the interpretation of the origin of different aspects, including the well known potential ambiguities, are of crucial importance for finding and justifying the procedures used for predicting nucleus-nucleus OMP in the era of radioactive nuclear beams (RNB) see e.g. [1]. The reliability of these potentials is essential for the correct description of a number of reactions involving RNBs, from elastic to nucleon transfer and nucleon removal, at energies ranging from a few to a few hundred MeV/nucleon. The folding model is central to this understanding, coupled with increased insight into the nature of realistic effective nucleon-nucleon interactions. Of particular interest for us is to support the absolute values of the calculated cross sections for reactions used in indirect methods for nuclear astrophysics, see [2] and [3] for the most recent results. In this

framework, we treat here the case of heavy ion orbiting, one of the phenomena found over the years to occur in special cases of elastic scattering, well understood semiclassically, but not well documented by specific examples.

In Sect. 2 we remind the basic ingredients of the double folding model. Sect. 3 is devoted to the analysis of ^{4}He+^{16}O at 54.1 MeV. In Sect. 4 the reaction ^{4}He+^{28}Si at 18 MeV is discussed. Our conclusions are presented in Sect. 5.

2. FOLDING FORMFACTORS

In the following we discuss the ability of the folding model to describe orbiting/resonant elastic scattering. We start by a quite simple model in which the spin-isospin independent formfactor of the OMP is given by the double folding integral,

$$V_{fold}(R) = \int d\vec{r}_1 d\vec{r}_2 \rho_1(r_1)\rho_2(r_2) v_{M3Y}(s) \tag{1}$$

where v_{M3Y} is the M3Y parametrization of the G-matrix obtained from the Paris NN interaction [4], and $\vec{s} = \vec{r}_1 + \vec{R} - \vec{r}_2$ is the NN separation distance. A small isovector component arising from a nonnegligible neutron skin is added if necessary. The Coulomb component of the optical potential is calculated by replacing the nuclear s.p. densities with proton densities and using $v_{coul}(s) = e^2/s$ as effective interaction. The small effect arising from finite proton size is ignored. In the simplest version of this model, dubbed here as M3YZR, the knockon exchange component is simulated by a zero range potential with a slightly energy dependent strength,

$$J_{00}(E) = -276(1 - 0.005E/A) \tag{2}$$

We keep the number of fitting parameters at the minimum level and take the OMP in the form,

$$U(R) = N_V V(R, t_V) + iN_W V(R, t_W) \tag{3}$$

where $N_{V,W}$ are normalization constants and $t_{V,W}$ are range parameters defined by the scaling transformation,

$$V(R, t) \rightarrow t^3 V_{fold}(tR) \tag{4}$$

This transformation conserves the volume integral of the folding potential and modifies the radius as,

$$< R^2 >_V = \frac{1}{t^2} < R^2 >_{fold} \tag{5}$$

Thus the strength of the formfactor is controlled by the parameters $N_{V,W}$. Note that the transformation in Eq. (4) ensures that only the rms radius of the bare folding potential is changed. This is in line with the original prescription of [5] which proposed a smearing procedure in terms of a normalized Gaussian function. We found that the

transformation in Eq. (4) is more efficient and less time consuming. Based on Eq. (5) one may estimate in an average way the importance of the dynamic polarization potential (DPP) and finite range effects. Throughout this paper we use single particle densities obtained from a spherical Hartree-Fock (HF+BCS) calculation based on the density functional of Beiner and Lombard [6]. The obtained rms charge radii are very close to the experimental values [7]. A more elaborate calculation leads to a nonlocal knockon exchange kernel [8],

$$U_{ex}(\vec{R}^+,\vec{R}^-) = \mu^3 v_{ex}(\mu R^-)\int d\vec{X}_1\rho_1(X_1)\hat{j}_1\left(k_{f1}(X_1)\frac{(A_1-1)A_2}{A_1+A_2}R^-\right) \quad (6)$$
$$\times\rho_2(|\vec{R}^+-\vec{X}_1|)\hat{j}_1\left(k_{f2}(|\vec{R}^+-\vec{X}_1|)\frac{(A_2-1)A_1}{A_1+A_2}R^-\right)$$

where $A_{1,2}$ are mass numbers, μ is the reduced mass of the system, $k_{f1,2}$ are Fermi momenta, $R^{+,-}$ are the usual nonlocal coordinates and v_{ex} is the exchange component of the interaction including the long range OPEP tail. Eq. (6) already shows that the nonlocality is small and behaves as $\sim\mu^{-1}$. In the lowest order of the Perey-Saxon approximation, the local equivalent of the nonlocal kernel is obtained by solving the nonlinear equation,

$$U_L(R) = 4\pi\int d\vec{r}_1 d\vec{r}_2\rho_1(r_1)\rho_2(r_2)$$
$$\times\int s^2 ds v_{ex}(s)\hat{j}_1(k_{f1}(r_1)\beta_1 s)\hat{j}_1(k_{f2}(r_2)\beta_2 s)$$
$$\times j_0\left(\frac{1}{\mu}K(R)s\right)\delta(\vec{r}_2-\vec{r}_1+\vec{R}) \quad (7)$$

Above $\beta_i=(A_i-1)/A_i$ are recoil corrections, $\hat{j}_1(x)=3j_1(x)/x$ and $j_{0,1}$ are spherical Bessel functions. The local Fermi momenta k_f are evaluated in an extended Thomas-Fermi approximation [9]. We have explored also the extended Slater approximation for the mixed densities of Campi and Bouyssy [10] but did not obtained substantial improvements over the usual Slater approximation. The local momentum for the relative motion is given by,

$$K^2(R) = \frac{2\mu}{\hbar^2}(E_{c.m.}-U_D(R)-U_L(R)) \quad (8)$$

where U_D is the total direct component of the potential including the Coulomb term. In Eq. (8) we assumed a purely real local momentum of the relative motion since the absorptive component of the OMP is small compared with the real part. The effective mass correction [11], $\frac{\mu^\star}{\mu}=1-\frac{\partial U}{\partial E}$ is of the order of a few percent for our systems and is absorbed in the renormalization parameter N_W. Some tens of iterations are needed to solve the coupled Eq. (7) and (8) in order to obtain a precision of 10^{-7} in the entire radial range ($R_{max}=25$fm). We start the iteration process by using

$U_L^{(0)} = U_D$. Calculations with finite range model are dubbed M3YFR. Neglecting the spin-orbit component, the Gogny NN effective interaction can be expressed as a sum of a central, finite range term and a zero range density dependent term,

$$v(\vec{r}_{12}) = \sum_{i=1}^{2}(W_i + B_i P_\sigma - H_i P_\tau - M_i P_\sigma P_\tau)e^{-\frac{r_{12}^2}{\mu_i^2}} \\ +t_3(1+P_\sigma)\rho^\alpha(\vec{R}_{12})\delta(\vec{r}_{12}) \tag{9}$$

where $\vec{r}_{12} = \vec{r}_1 - \vec{r}_2$, $\vec{R}_{12} = (\vec{r}_1 + \vec{r}_2)/2$ and standard notations have been used for parameter strengths and spin-isospin exchange operators. The strengths parameters and the ranges are taken from [12]. The isoscalar and isovector components of the effective interaction are constructed in the standard way. The interest in this interaction resides in its excellent description (at the HF level) of the saturation properties of the nuclear matter in line with modern estimation from the isoscalar giant monopole [13] or dipole resonance [14] studies. Antisymmetrization of the density dependent term is trivial, so that the sum of direct and exchange term reads,

$$v_D^\rho(r_{12}) + v_{ex}^\rho(r_{12}) = \frac{3t_3}{4}\rho^\alpha\delta(\vec{r}_{12}) \tag{10}$$

The local equivalent of the finite range knockon exchange is calculated with Eq. (7). Two approximations were used for the overlap density,

$$\rho = (\rho_1(r_1)\rho_2(r_2))^{1/2} \tag{11}$$

and

$$\rho = \frac{1}{2}(\rho_1(r_1) + \rho_2(r_2)) \tag{12}$$

The first approximation Eq. (11) has the merit that the overlap density goes to zero when one of the interacting nucleons is far from the bulk. In Eq. (12) a factor 1/2 was introduced such as the overlap density does not exceeds the equilibrium density for normal nuclear matter. At large density overlaps, the fusion and other inelastic processes are dominant and the elastic scattering amplitude is negligible small. The calculated OM potentials are dubbed GOGNY1 (11) and GOGNY3 (12). Both definitions represent crude approximations of the overlap density but are widely used in the estimation of the density dependence effects in the folding model. We further examine the density dependence effects by using the nuclear matter approach of Jeukenne, Lejeune and Mahaux (JLM) [5] which incorporates a complex, energy and density dependent parametrization of the NN effective interaction obtained in a Brueckner Hartree-Fock approximation from the Reid soft core NN potential. The systematic study [1] of the elastic scattering between p-shell nuclei at energies around 10 MeV/nucleon leads to the surprising result that on average, the imaginary part of the folded JLM potential was perfectly adequate to describe such reactions and

did not need any renormalization ($N_W = 1.00 \pm 0.09$), while the real component needed a substantial renormalization, in line with other effective interactions used in folding models. We examine here to which extent this feature is conserved for tightly bound nuclei. Exchange effects are included in this model at the level of N-target interaction. Calculations with this model are dubbed JLM1 and JLM3, depending on which definition we use for the overlap density (Eqs.(11) and (12) respectively).

3. ^{4}HE+^{16}O AT 54.1 MeV

The reaction ^{4}He+^{16}O at E_{lab}= 54.1 MeV was measured by Abele *et al.* [15] and discussed extensively within the folding model in [16]. An optical potential description of both α+^{16}O elastic scattering and α-cluster states in ^{20}Ne was given by Michel *et al.* [17]. The corresponding global potential α+^{16}O gives a reasonable description of the α-structure in ^{20}Ne. However such a global approach cannot be used to reveal a delicate phenomenon such as orbiting. A more detailed analysis is necessary.

Table 1
Discrete solutions with WS^1 form factors for the reaction ^{4}He+^{16}O at 54.1 MeV.

V	W	r_V	r_W	r_c	a_V	a_W	χ^2	σ_R	J_V	R_V	J_W	R_W
135.	10.57	0.7231	1.0741	1.0	0.8022	0.6867	8.72	1050.	399.	3.7646	74.	4.2654
160.	18.17	0.8773	0.9618	1.0	0.5993	0.5083	7.87	999.	624.	3.5712	85.	3.5963
214.	24.42	0.9104	0.9553	1.0	0.5066	0.1188	7.72	986.	865.	3.4548	97.	3.0712

Table 2
Unique solution with WS^2 form factors for the reaction ^{4}He+^{16}O at 54.1 MeV.

V	W	r_V	r_W	r_c	a_V	a_W	χ^2	σ_R	J_V	R_V	J_W	R_W
155.	14.75	0.9088	1.1628	1.0	1.2026	1.0812	4.19	1028.	393.	3.6687	75.	4.0902

A grid search using standard WS^1 formfactors for the optical potential revealed a number of discrete solutions, see Table 1 and Figure 1a. Although almost all physical angular range was measured the data are not able to fix uniquely the potential of a WS shape. The members of the potential family are very strong, reaching high values of the normalized real volume integral. The rms radii of the real and imaginary component get smaller as the potential is stronger. However the reaction cross section is almost constant which suggests that the members of the potential sequence are almost phase equivalent. Examination of the Figure 2a shows quite similar cross section with the exception of the solution with $J_v = 399$ MeV fm^3 which show a very deep Airy oscillation near $\theta = 60^\circ$ just at the end of the Fraunhofer sector. This structure which is followed by a wide bump together with the far side dominance is

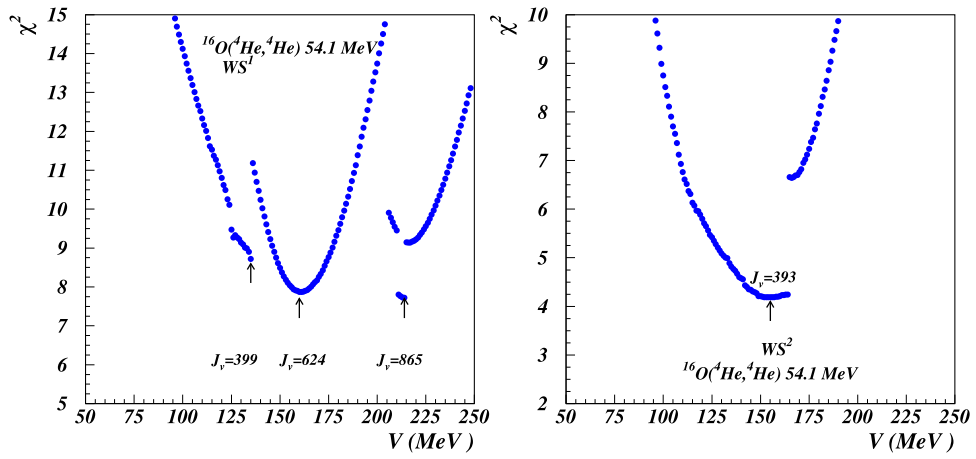

Fig. 1 – (Color online) Grid search with WS^1(a) and WS^2(b) form factors for the reaction ^{4}He+^{16}O at 54.1 MeV, Table 1.

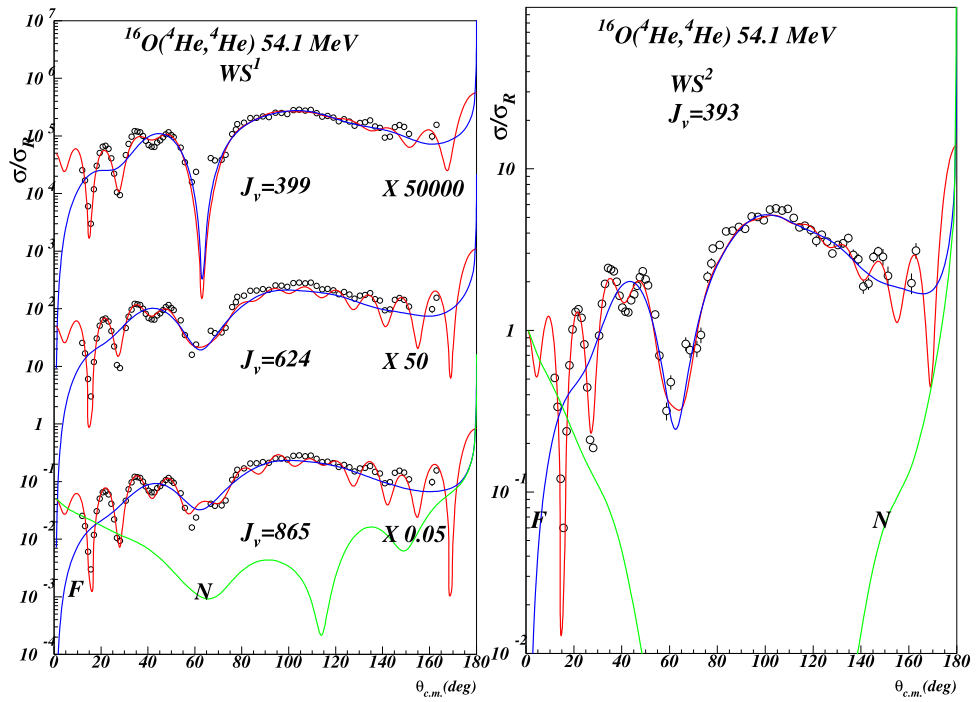

Fig. 2 – (Color online) F/N decomposition for the WS^1(a) and WS^2(b) potentials.

usually interpreted a a strong refractive effect of a quite transparent potential. This picture has been already challenged by Anni [18] for the simple reason that the far side amplitude has never been decomposed into subamplitudes which would explain the interference. A subsequent analysis in terms of WS^2 formfactors (squared WS) revealed a single solution in the range $J_v < 1000$ MeV fm^3, see Table 2 and Figure 1b. The uniqueness of the solution cannot be guaranteed by our search procedure. Remarkably, the WS^2 solution and the first WS^1 solution in Table 1 have almost identical bulk average parameters (volume integrals, rms radii and reaction cross section) which suggests that this is the physical solution. The far and near side (F and N) amplitudes have the same structure with a deep Airy oscillation carried entirely by the far side component. We shall use later this solution for our semiclassical analysis.

Table 3
Unique solutions obtained with folding form factors for the reaction ^{4}He+^{16}O at 54.1 MeV

pot	N_V	N_W	t_V	t_W	χ^2	σ_R	J_V	R_V	J_W	R_W
M3YZR	0.8400	0.1718	1.0178	0.8536	4.63	1083.	374.10	3.603	75.61	4.286
M3YFR	0.8250	0.1689	1.0020	0.8887	4.94	1069.	397.46	3.661	80.70	4.120
GOGNY1	0.6850	0.1420	1.0143	0.9147	5.81	1057.	401.73	3.657	82.67	4.049
GOGNY3	0.8800	0.1830	1.0278	0.9340	6.05	1058.	406.87	3.666	84.06	4.029
JLM1	0.6750	0.5947	0.9620	0.8801	4.23	1037.	391.99	3.626	77.48	4.076
JLM3	0.7250	0.6736	0.9577	0.8773	4.27	1042.	388.28	3.619	76.96	4.107

In the folding model we use three different effective interactions, namely the density independent M3Y, and two density dependent GOGNY and JLM in six different versions. A grid search using the strength N_v as a control parameter revealed a unique solution for all model interactions. We have obtained an almost unique shape for the function $\chi^2(J_v)$ see Table 3 and Figure 3. The folding solutions are fully consistent with the WS model. The average real volume integral is $J_v = 392 \pm 18$ MeV fm^3 and the real rms radius $R_v = 3.65 \pm 0.02$ fm. The normalization for the real component ranges from $N_v \approx 0.7$ to $N_v \approx 0.9$ strengthen once again the conjecture that the true physical parameter is the volume integral and not the normalization parameter. A standard far side/near side decomposition is plotted in Figures 4a and 4b showing the same far side dominance and an Airy minimum forward to a "rainbow" bump. There are some glories at very large angles due to a strong F/N interference since both amplitudes become large in this sector. We start a WKB analysis [19] by searching the turning point trajectories in the complex r plane. We use the WS^1 potential with real volume integral $J_v = 399$ MeV fm^3. We observe an ideal situation with three active well separated turning points close to the real axis, Figure 5a. The active points, which give the essential contribution to the action integrals are correlated with the poles of the real component of the optical potential (left hand stars in

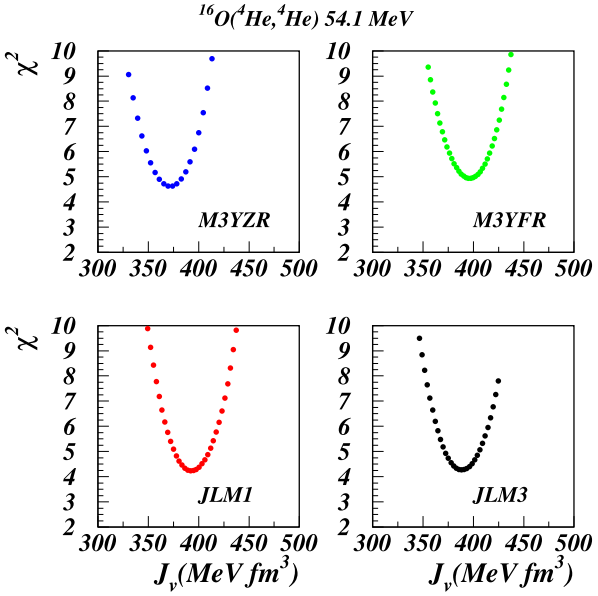

Fig. 3 – (Color online) Grid search with folding form factors. Unique solution, Table 3

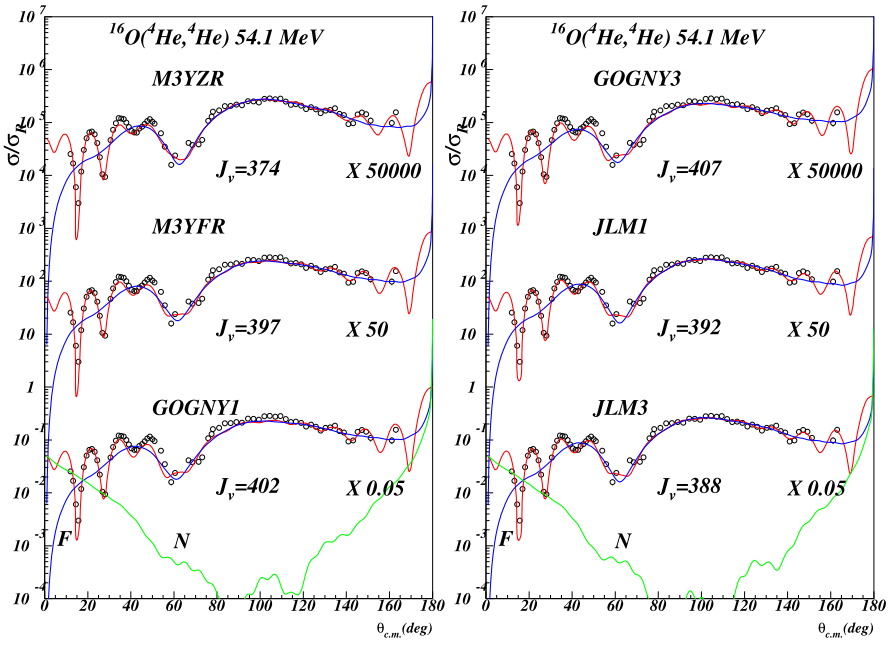

Fig. 4 – (Color online) F/N decomposition for the folding potentials from Table 3.

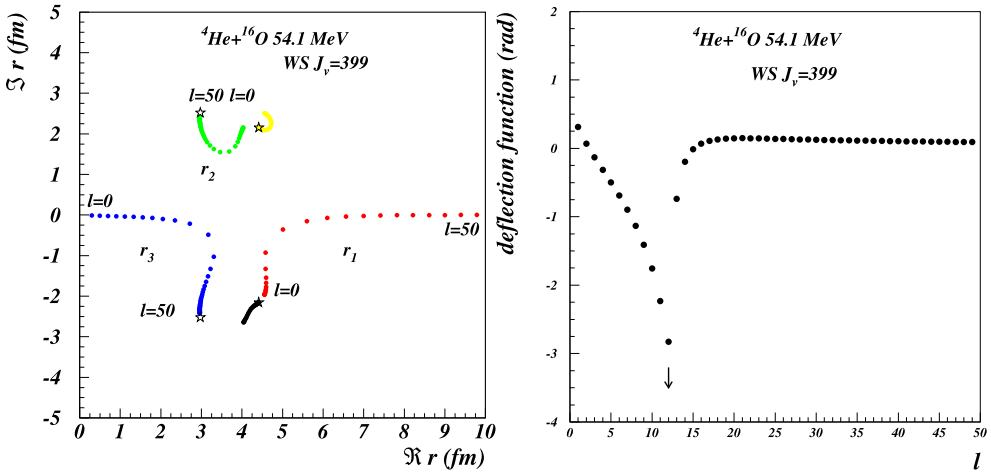

Fig. 5 – (Color online) (a) Complex turning points for the WS potential with $J_V = 399$ MeV fm^3. (b) Semiclassical deflection function for the WS potential with $J_V = 399$ MeV fm^3. The pattern is close to a near orbiting situation with the orbiting momentum $\ell \sim 12$.

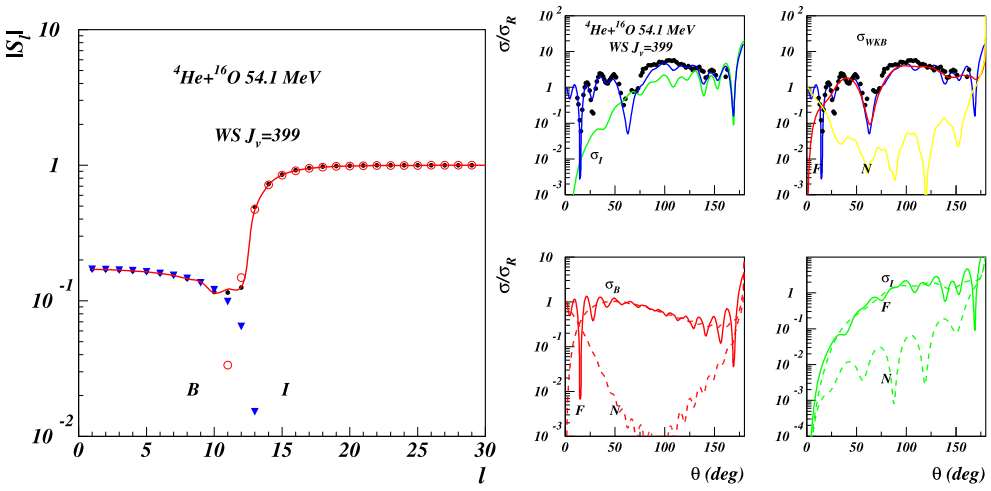

Fig. 6 – (Color online) (a) Absorption profile for the WS potential with $J_V = 399$ MeV fm^3 (see text). (b) Semiclassical (WKB) analysis of the reaction ^{4}He+^{16}O at 54.1 MeV based on the WS potential with $J_V = 399$ MeV fm^3 (see text).

the figure). The inactive turning points are correlated with the poles of the imaginary potential and give negligible small contribution to the action integrals. The semiclassical deflection function is shown in Figure 5b. There are at most 20 partial waves which contribute significantly to the scattering. The Coulomb rainbow is embedded

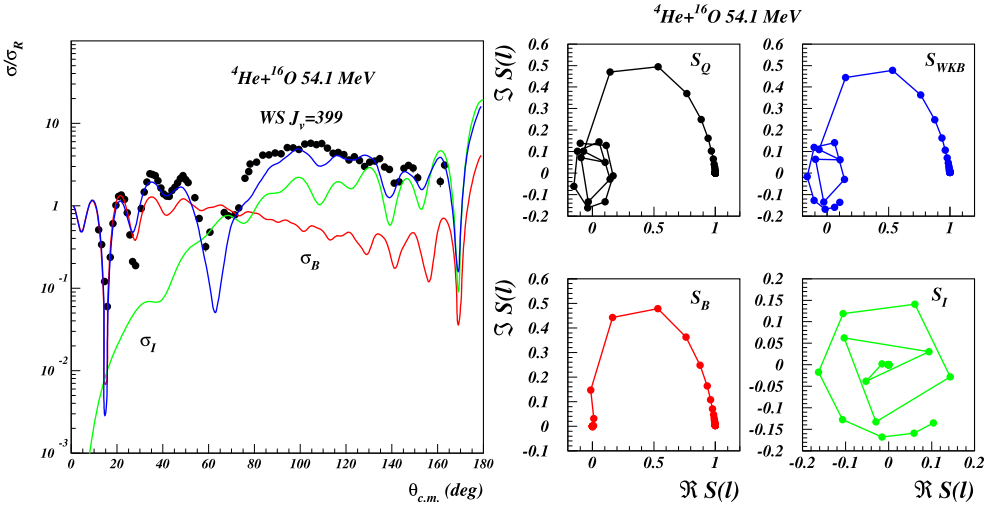

Fig. 7 – (Color online) (a) The semiclassical (WKB) cross section is decomposed into barrier (B, red line) and internal barrier (I, green line). The deep Airy minimum appears as a strong interference of the B/I components. The internal barrier component dominates at large angles, reaching exceptionally large values ($\sigma_I/\sigma_R \sim 20$ at $\theta \sim 180^\circ$). (b) Argand diagram for the semiclassical S-matrix based on the WS potential with $J_V = 399$ MeV fm^3. The trajectory for the S_{WKB} matches perfectly the exact quantum result S_Q. The internal barrier component, which reaches exceptionally large values, rotates several times around the origin suggesting the orbiting.

in the Fraunhofer sector. Clearly there is a logarithmic singularity near $l_{orb} = 12$ and therefore the reaction is dominated by orbiting. The semiclassical absorption profile (modulus of the scattering amplitude as a function of the angular momentum) is shown in Figure 6a. The semiclassical profile (curve) is identical with the exact quantum-mechanically result (black dots) which strengthen the conjecture that the WKB decomposition of the scattering amplitude is exact, at least for this reaction. The internal barrier component (I) is quite large, characteristic for strongly refractive reactions [20] and is negligibly small beyond the orbiting momentum. The barrier (B) and internal barrier (I) components of the scattering amplitude interfere destructively giving rise to a shallow Grühn-Wall dip near the orbiting momentum. The semiclassical (WKB), barrier (B) and internal barrier (I) cross sections as well as their far side/near side subcomponents are shown in Figures 6b and 7a. The barrier component (left lower panel) is responsible for the diffractive Fraunhofer sector and becomes again significant near $\theta = 180^\circ$. The internal barrier component (right lower panel) is significant at all intermediate angles and the destructive interference with the barrier component explains the Airy minimum near $\theta = 60^\circ$. The internal barrier cross section is exceptionally large near $\theta = 180^\circ$ where $\sigma^I/\sigma_R = 20$. Finally, the Argand diagram for the semiclassical (WKB) S-matrix is shown in Figure 7b.

The exact quantum result (Q) is shown for comparison. The WKB S-matrix is decomposed into barrier (B) and internal barrier (I) components. The orbiting/resonant effect is evident in the low partial waves sector. The barrier component is free for resonances. The entire resonant effect is isolated into the internal barrier component (right lower panel) where the S-matrix rotates anti-clockwise several times around the origin. These are resonances /Regge poles of the orbiting mechanism.

Table 4
Discrete solutions with folding form factors for the reaction ^{4}He+^{28}Si at 18.0 MeV.

pot	N_V	N_W	t_V	t_W	χ^2	σ_R	J_V	R_V	J_W	R_W
M3YZR	0.4900	0.0673	0.8469	0.9997	4.47	1183.	220.80	4.649	30.63	3.946
	0.7450	0.0581	0.8675	1.2983	6.58	1287.	336.18	4.540	27.00	3.051
M3YFR	0.4300	0.0647	0.8750	1.1067	4.49	1141.	210.15	4.572	32.09	3.627
	0.6650	0.0539	0.8971	1.1402	6.13	1233.	325.48	4.461	26.78	3.522
GOGNY1	0.3600	0.0564	0.8900	1.1525	4.69	1138.	208.14	4.541	33.18	3.520
	0.5550	0.0432	0.9126	1.2495	5.64	1215.	321.34	4.430	25.58	3.251
JLM1	0.3550	0.2354	0.8367	1.1387	4.19	1143.	212.48	4.568	30.92	3.629
	0.5450	0.1889	0.8560	1.3226	5.92	1242.	326.64	4.466	25.09	3.133
JLM3	0.3900	0.3019	0.8321	1.1436	4.20	1138.	212.10	4.572	30.29	3.642
	0.6000	0.2502	0.8527	1.3011	6.10	1241.	326.77	4.463	25.35	3.209

Table 5
Discrete solutions with WS[1] form factors for the reaction ^{4}He+^{28}Si at 18.0 MeV.

V	W	r_V	r_W	r_c	a_V	a_W	χ^2	σ_R	J_V	R_V	J_W	R_W
53.	3.44	0.9174	1.2304	1.0	0.9271	0.2423	4.43	1089.	223.	4.7611	24.	4.4982
88.	4.70	0.8756	1.2234	1.0	0.8542	0.2368	5.08	1140.	314.	4.4623	32.	4.4693
128.	5.70	0.8550	1.2244	1.0	0.7962	0.2270	5.45	1159.	414.	4.2585	39.	4.4659

Table 6
Unitary solutions with Regge pole amplitudes for the reaction ^{4}He+^{28}Si at 18.0 MeV.

Set	L	Δ	α	β	L_1	Δ_1	D_1	Γ_1	L_2	Δ_2	D_2	Γ_2	χ^2	σ_R
R1	8.14	4.00	-1.66	2.13	7.73	0.415	10.3	20.6	8.68	0.204	10.9	2.61	2.64	1680
R2	7.85	4.16	-1.67	2.37	7.98	0.421	13.6	27.4	8.06	0.413	11.3	1.38	2.69	1703

4. ^{4}HE+^{28}SI AT 18 MEV

We discuss here another reaction, ^{4}He+^{28}Si at $E_{lab} = 18$ MeV measured by Ahlfeld *et al.* [21]. The incident energy is quite low, just at the limit where the reaction mechanism starts to be dominated by direct interactions over compound elastic. The interest in this reaction resides in the fact that it displays a special kind

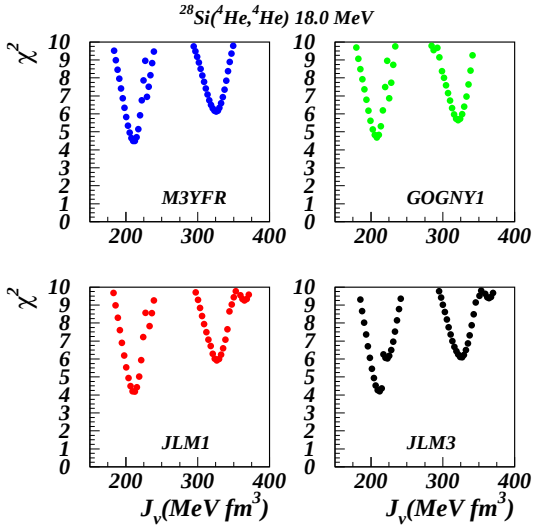

Fig. 8 – (Color online) Search for discrete solutions with folding form factors.

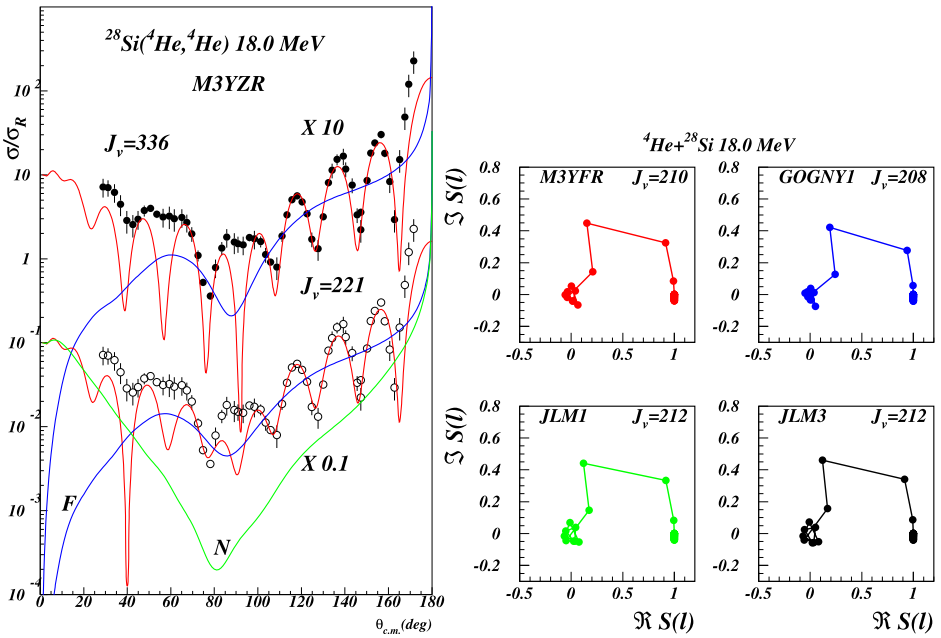

Fig. 9 – (Color online) (a) F/N decomposition with M3YZR. There are normalization problems at forward angles. (b) Argand diagram for the S-matrix calculated with several folding solutions with real volume integral $J_V \sim 210$ MeV fm^3.

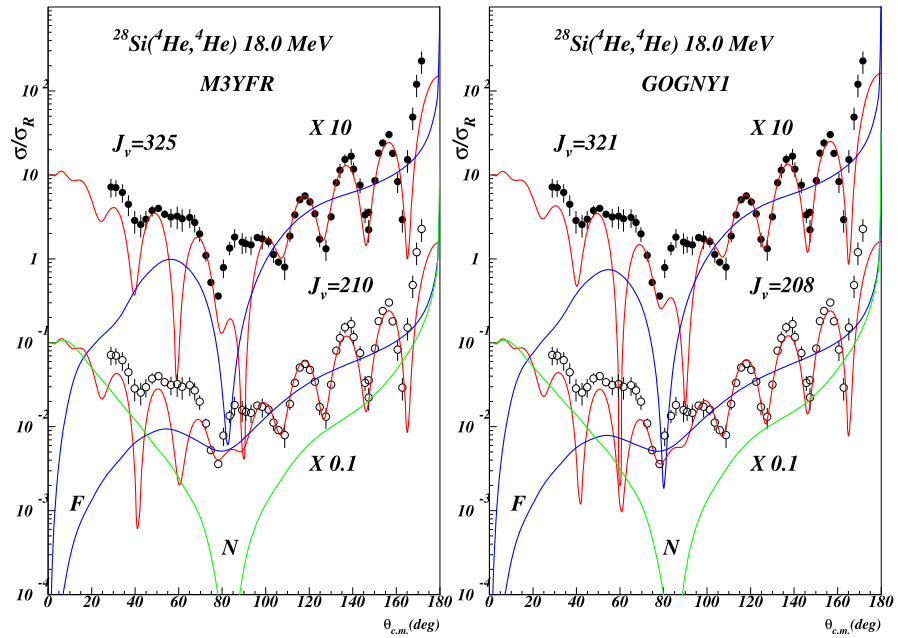

Fig. 10 – (Color online) (a) F/N decomposition with M3YFR. (b) F/N decomposition with GOGNY1.

of orbiting-butterfly scattering. The angular distribution is almost symmetric with respect to $\theta = 90^\circ$ and displays diffractive oscillations in the entire physical angular range. Our analysis go through the same steps as for the preceding reaction. Since the energy is quite low, we expect a significant number of discrete solutions with both WS and folding optical potentials see Tables 4 and 5. The χ^2 landscape is explored in Figures 8 and 12b. Remarkably two solutions with $J_v \approx 200$ MeV fm^3 and $J_v \approx 300$ MeV fm^3 appear in all six model calculations. The far side/near side decomposition is shown in Figures 9a-11b and 13a. For all solutions there is a clear far side dominance and a particularly deep Airy minimum near $\theta = 80^\circ$ for the solution with $J_v \approx 300$ MeV fm^3. This should in principle indicates a strongly refractive reaction mechanism. But we shall see that is not the case. The first hint is given by the large angle oscillations which can be fitted by a renormalized $P_8^2(\theta)$ amplitude which suggests the presence of a Regge pole near $\ell = 8$ For the moment we are interested if there are other traces of resonant scattering in our reaction. We show the Argand diagram for the folding S-matrix in Figure 9b. The figure shows convincingly that the corresponding folding potentials are phase equivalent since the S-matrix trajectories in angular momentum space are identical. Second, there is a cluster of points in the low angular momentum sector which in fact is a signature of the orbiting. The absorption profile for the same S-matix are shown in Figure 12a. There is a signif-

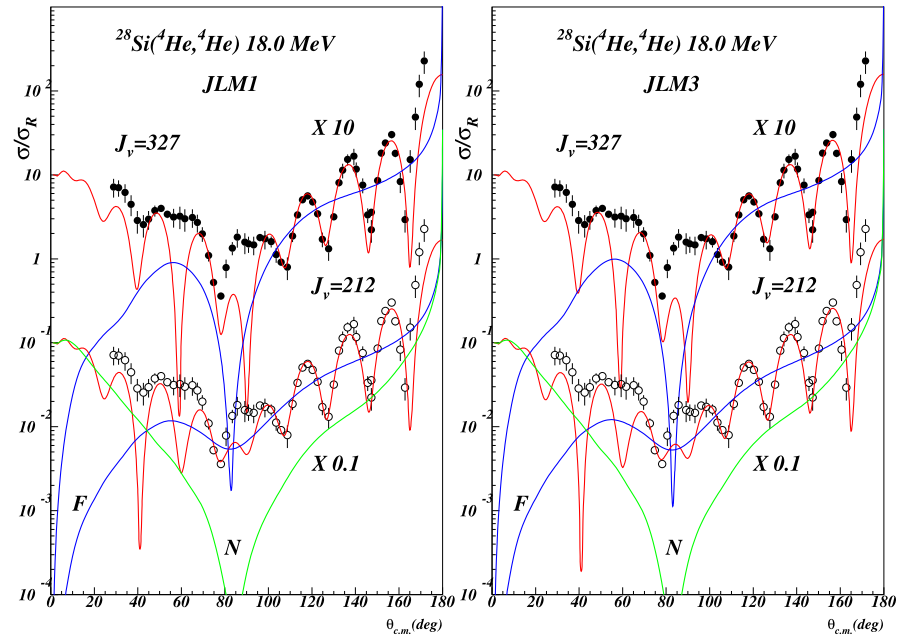

Fig. 11 – (Color online) F/N decomposition with JLM1(a) and JLM3(b).

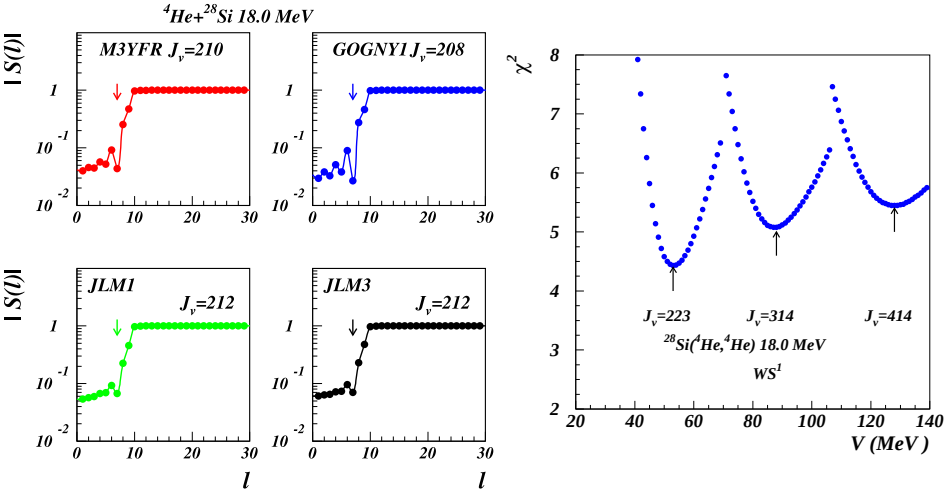

Fig. 12 – (Color online) (a) Absorption profile calculated with several folding solutions. The arrows indicate the position of the Regge pole. (b) Search for discrete solutions with WS^1 form factors.

icant odd-even staggering at low partial waves (multiple Regge poles). The arrow indicates the location of the main Regge pole near $\ell = 8$. The trajectories of the

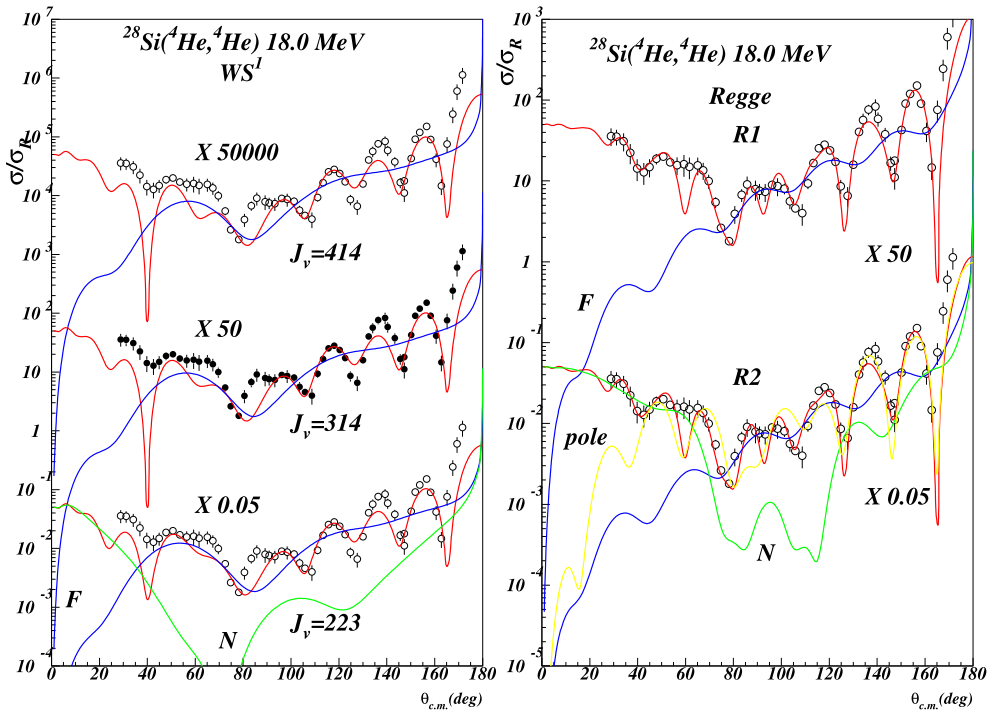

Fig. 13 – (Color online) (a) F/N decomposition with WS[1]. This calculation did not solved the normalization problem at forward angles. (b) F/N decomposition using Regge pole amplitudes. The pole components dominate the cross section in the entire angular range.

complex turning points for the WS[1] potential with $J_v = 223$ MeV fm^3 are shown in Figure 14b. The barrier turning point r_2 and the outer point r_1 have an unusual trajectory shape due to the fact that the imaginary component of the optical potential has complex poles located close to the real axis (right hand stars), see in Table 5 potentials with very small a_w. The calculation of the action integrals requires a careful numerical evaluation since the poles should be avoided. Figure 15a displays the semiclassical deflection function with a typical orbiting singularity near $\lambda = 9.5$. The semiclassical absorption profile, shown in Figure 15b, indicate a quite strong internal barrier component. The semiclassical profile do not reproduce the exact Grühn-Wall spike (black dots) but still appears as a B/I interference near the orbiting momentum. The internal barrier component (I) is negligibly small beyond the orbiting momentum. The semiclassical cross section are calculated and displayed in Figure 16a. The barrier component, typical for strong absorption, follows quite well the experimental cross section, though it is the internal barrier component which dominates the cross section at large angles. The Argand diagram shown in Figure 16b shows a strong

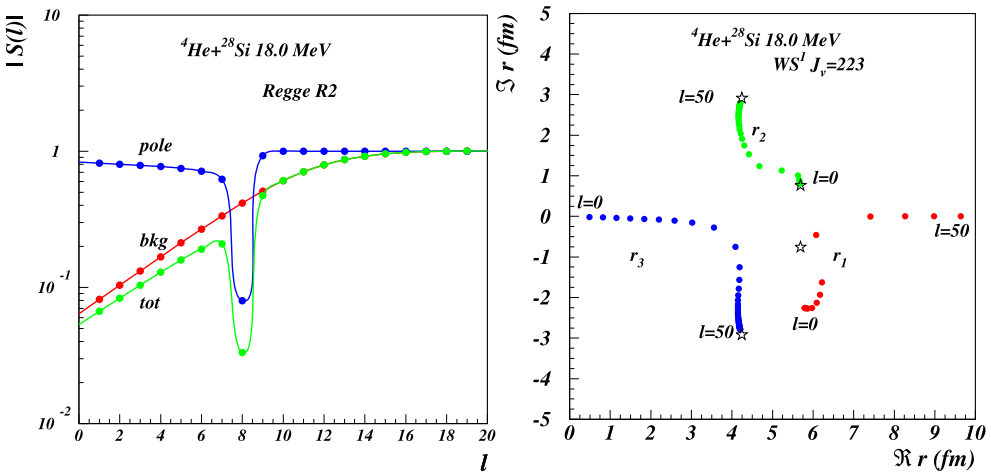

Fig. 14 – (Color online) (a) Absorption profile using Regge pole amplitude R2. The main pole located near $\ell = 8$ produced a deep Grühn-Wall spike in the total S-matrix. (b) Complex turning point trajectory for the WS^1 potential with real volume integral $J_V = 223$ MeV fm^3.

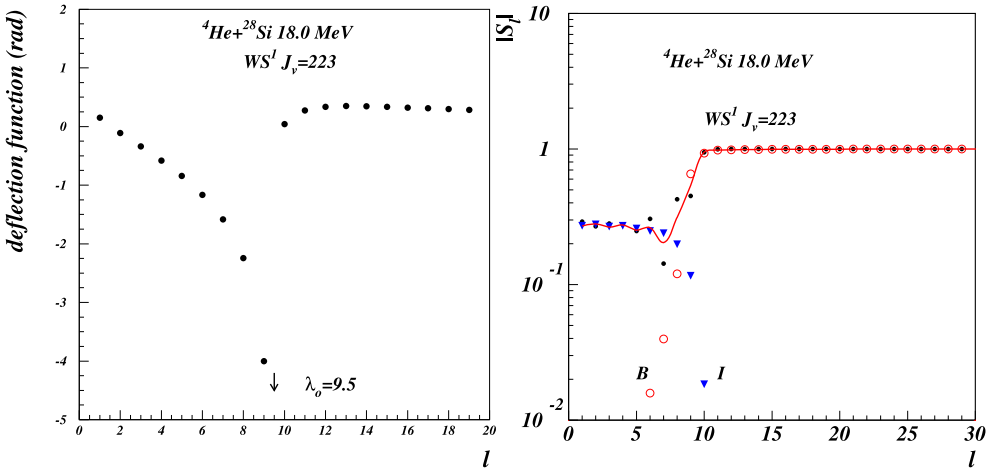

Fig. 15 – (Color online) (a) Deflection function. The orbiting angular momentum is $\lambda_0 = 9.5$. (b) Semiclassical (WKB) absorption profile red curve. The quantum mechanical solution (black dots) is shown for comparison. The WKB solution is decomposed into barrier (B) and internal barrier (I) components.

orbiting effect in both semiclassical (WKB) and quantum (Q) S-matrix. The entire resonant effect is isolated into the internal barrier component (I). Finally we search the Regge poles directly from the data. We proceed as follows: we guess a reasonable background-two pole solution, as described in the preceding paper and then generate

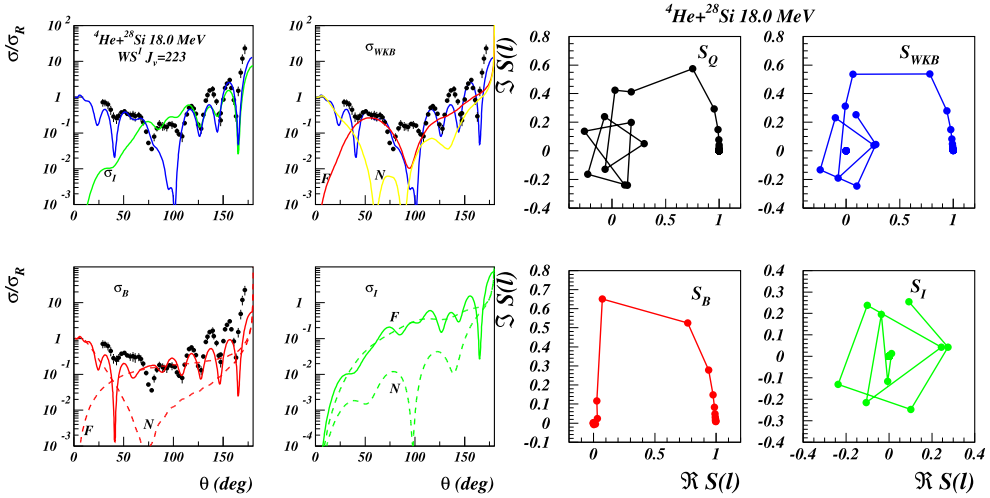

Fig. 16 – (Color online) (a) Semiclassical (WKB) cross section compared with the data. The regular oscillations at large angles are triggered by the barrier component. But their amplitude is determined by the internal barrier component (green curve). The B/I components are further decomposed into F/N subcomponents. (b) Argand diagram for the semiclassical (WKB) S-matrix is compared with the exact quantum mechanical result (Q). The orbiting effect is isolated into the internal barrier component (I).

about 10^6 input solution by Monte Carlo for our searching code which minimizes a standard χ^2 function. We are looking for solutions for which both the background and the pole component are unitary, since we want to isolate the pole contribution to the cross section. Two fully unitary solutions are given in Table 6 and confirms the preceding analysis with a main pole located near $\lambda = 8$. The cross sections obtained with this model are plotted in Fig.13b. The butterfly effect is even more evident in this calculation The background component is important only at forward angles, while the pole component contributes significantly at all angles. The background absorption profile shown in Fig. 14a is typical for strong absorption regime while the Grühn-Wall spike of exceptional amplitude appears here as carried out by the pole component alone.

5. CONCLUSION

We have analyzed here two apparently obscure angular distribution for heavy ion scattering which proved to be extremely rich in information about the reaction mechanism. The first example α+^{16}O at 54.1 MeV show all characteristics of a strongly refractive reaction but proves to be in fact a typical example of heavy ion orbiting. A second example, α+^{28}Si at 18.0 MeV taken at the limit where the direct interaction starts to dominate over the compound elastic, show a special case of heavy

ion orbiting, butterfly scattering with diffractive oscillations in the entire physical angular range due to Regge pole dominance. In the light of our analysis it is evident that a lot of reactions dubbed improperly as ALAS (strong increase of the cross section at large angles) should be reanalyzed since most if not all of them could be in fact cases of nuclear orbiting.

Acknowledgements. This work was partly supported by CNCSIS Romania, under program PN-II-PCE-55/2011 and PN-II-ID-PCE-0299/2012, and partly by IN2P3, France.

REFERENCES

1. L. Trache, A. Azhari, H. L. Clark, C. A. Gagliardi, Y.-W. Lui, A. M. Mukhamedzhanov, X. Tang, N. Timofeyuk, R. E. Tribble and F. Carstoiu, Phys. Rev. **C61**, 024612 (2000).
2. T. Al-Abdullah, F. Carstoiu, X. Chen, H. L. Clarke, C. A. Gagliardi, Y.-W. Lui, A. Mukhamedzhanov, G. Tabacaru, Y. Takimoto, L. Trache, R.E.Tribble, Y. Zhai Phys. Rev. C **89**, 025809 (2014).
3. T. Al-Abdullah, F. Carstoiu, C. A. Gagliardi, G. Tabacaru, L. Trache and R. E. Tribble. Phys. Rev. C **89**, 064602 (2014).
4. N. Anantaraman, H. Toki and G. F. Bertsch, Nucl. Phys. **A398**, 269 (1983).
5. J. P. Jeukenne, A. Lejeune and C. Mahaux, Phys. Rev. **C16**, 80 (1977).
6. M. Beiner and R. J. Lombard, Ann. Phys. (N.Y.) **86**, 262 (1974).
7. I. Angeli, Heavy Ion Physics, **8**, 23 (1998).
8. F. Carstoiu and M. Lassaut, Nucl. Phys. **597**, 269 (1996).
9. Dao T. Khoa, Phys. Rev. **C63**, 034007 (2001).
10. X. Campi and A. Bouyssy, Phys. Lett. **73B**, 263 (1978).
11. J. W. Negele and K. Yazaki, Phys. Rev. Lett. **47**, 71 (1981).
12. D. Gogny, *Proc. Int. Conf. on Nucl. Physics, Munich 1973, eds J. de Boer and H. J. Mang, Vol. 1, p. 48.*
13. D. H. Youngblood, H. L. Clark and Y.-W. Lui, Phys. Rev. Lett. **82**, 691 (1999).
14. G. Colo, N. Van Giai, P. F. Bortignon and M. R. Quaglia, Phys. Lett. **B485**, 362 (2000).
15. H.Abele, H.J.Hauser, A.Korber, W.Leitner, R.Neu, H.Plappert, T.Rohwer, G.Staudt, M.Strasser, S.Welte, M.Walz, P.D.Eversheim, F.Hinterberger, Z.Physik **A326** 373,1987.
16. H. Abele and G. Staudt, Phys. Rev. **C47**, 742 (1993).
17. F. Michel, J. Albinski, P. Belery, Th. Delbar, Gh. Gregoire, B.Tasiaux and G. Reidemeister Phys. Rev. **C28**, 1904 (1983).
18. R. Anni, Phys. Rev. C **63**, 031601R (2001).
19. D. M. Brink and N. Takigawa, Nucl. Phys. **A279**, 159 (1977).
20. Florin Carstoiu, Livius Trache, Robert E.Tribble, Carl A. Gagliardi Phys. Rev. **C70** 054610, (2004)
21. C. E. Ahlfeld, G. E. Assousa, R. A. Lasalle, W. J .Thompson, H. A. Van Rinsvelt, N. P. Heydenburg, Nucl. Phys **A191** 137(1972).